Stimuli-responsive assembly of nanoparticles with solid binding proteins

Yundi Zhao

A thesis

submitted in partial fulfillment of the

requirements for the degree of

Master of Science in Chemical Engineering

University of Washington

2019

Committee:

François Baneyx

David Castner

Program Authorized to Offer Degree:

Chemical Engineering

University of Washington

Abstract

Stimuli-responsive assembly of nanoparticles

with solid binding proteins

Yundi Zhao

Chair of the Supervisory Committee:
François Baneyx
Chemical Engineering

Solid binding peptides (SBPs) are short sequences of amino acids selected by combinatorial techniques for their high affinity for inorganic surfaces. When genetically encoded within proteins, SBPs can function as linkers to create hybrid materials comprising inorganic components and the proteins to which they are fused. In this project, we explored how such solid binding proteins may be employed to achieve dynamic control over the assembly and disassembly of silica nanoparticles and how the process is influenced by SBP sequence, insertion point, and solution conditions. Using fluorescent-resonant energy transfer (FRET), dynamic light scattering (DLS) and scanning electron microscopy (SEM), we show that bifunctional derivatives of superfolder green fluorescent protein (sfGFP) engineered with two strong, or with a strong and a weak silica-binding peptides support the pH-dependent aggregation and disaggregation of rhodamine-containing silica nanoparticle (RhSiNP). We further demonstrate that pH shifts can be used to cycle nanoparticle between assembled and dispersed states and that aggregate size can be tuned with different SBPs and salt concentrations. This new paradigm for the synthesis of dynamic nanoparticle systems should find applications in biosensing, diagnostics and advanced materials.

TABLE OF CONTENTS

ACKNOWLEDGEMENTS

I want to thank all the people that have supported and helped me during my master program at the University of Washington. First to my family who has encouraged me throughout this entire journey, accompanying me to overcome all the difficulties and inspiring me to always look forward. I'm also fully indebted to my professor François Baneyx for his guidance and help which has shaped my scientific mindset and encourage me to stay curious and keep exploring more unknown world in both research and life. In addition, I'm grateful to all of the people that I have known during the time, especially my lab members Jessica, Brittney, Alex, Julia, Matt, Jinrong and my best friend Liqian who have always been with me whenever I need help or just a sympathetic ear.

1. INTRODUCTION

1.1. Solid Binding Peptides and Car9 Variants

Biomineralization is a natural process in which living systems produces minerals for specific functions and protection support of living tissues.[1] Common biominerals include the silica walls of diatoms and the shells of mollusks which are made of calcium carbonate. Proteins often play a key role in these biomineralization processes. They are responsible for transporting, storing, precipitating and templating inorganic components.[2] Organized from the nano to the mesoscale, hybrid materials containing organic and inorganic components can have a finely tuned hierarchical structure determined by protein or peptide building blocks.

Research has shown that biomineralizing proteins used usually have a specific sequence responsible for inorganic precipitation. This has aroused people's interests in using synthetic proteins to mimic nature's outstanding control over the structure of inorganic materials. For decades, solid binding peptides (SBPs) have been used to study biotic-abiotic interactions and to organize organic and inorganic components for nanobiotechnology applications. SBPs are short stretches of amino acids, typically 7 to 12 residues long that are isolated by phage or cell surface display. They generally exhibit high selectivity and affinity to surfaces of inorganic materials,[3] and can be genetically fused to, or inserted within, larger protein frameworks. The process endows SBPs with higher stability and solubility. Furthermore, insertion of multiple SBPs within a single protein framework provides an ability to bind or mineralize several inorganic components to build complex architectures[4] that have been used in biomaterial production, nanostructure fabrication and biomedical applications.[5-7]

Car9 is a dodecapeptide of amino acid sequence DSARGFKKPGKR that was isolated via FliTrX cell surface display by Baneyx group. It was originally identified as a carbon-binding peptide that binds to carbonaceous substrates and exhibits a preference for sp^3-hybridized carbon.[8] Later, Car9 was shown to exhibit high affinity for silica (SiO_2) whose surface is terminated with negatively charged silanol (Si-OH) groups.[9, 10] Based on this silica-binding ability, a rapid and inexpensive affinity purification method was developed in which Car9 functions as an affinity tag that promote the binding of fused proteins to silica particles. Bound proteins can be eluted from the silica matrix with free lysine with a purity of 80-90%.[9] In addition, Car9 supports protein immobilization in sol-gels network and microcontact printing of fused proteins.[11, 12] Rosetta and MD simulation suggest that Car9's lysine (K) residues form a tripod-like structure projecting from a central core along with equatorial arginine (R) residues. These basic residues play an essential role in promoting interactions between Car9 and silica surfaces.[13]

Previous work in the Baneyx lab has focused on evaluating how the composition, conformation, and location of silica-binding peptides inserted at various positions of the super-folder green fluorescent protein (sfGFP) framework affect binding to silica. sfGFP was selected as a scaffold to explore protein-enabled nanoparticle assembly based on its high thermostability and high fluorescence compared to wild type (WT) GFP. In addition, the loop 9 of sfGFP (residues172−173) is permissive for the insertion of extraneous amino acid sequences. This site is opposite to the N- and C-termini (Figure 1a).[14] We therefore constructed a series of Car9-tagged sfGFP derivatives placing the Car9 sequence art different locations. In this project, we specifically focus on the C-terminus and loop 9 to produce sfGFP-Car9 (Figure 1b) and sfGFP::Car9 (Figure 1c). We also use an electrostatic mutant (K8AK11A) in which the 8th and 11th lysine residues are replaced with alanine that carries no net charge.

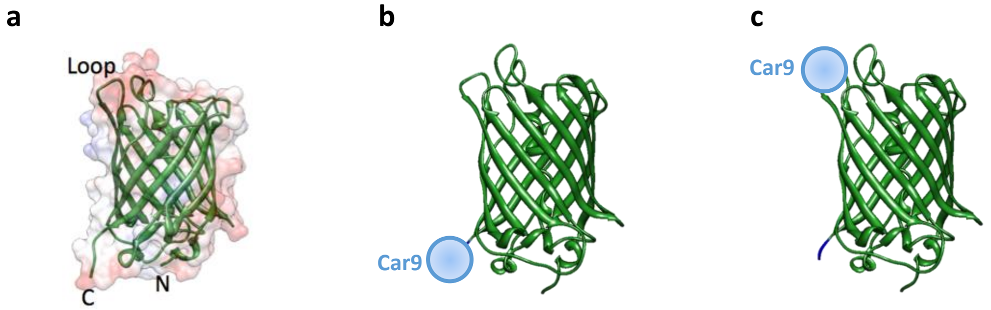

Figure 1. Structure of (a) WT sfGFP with N-terminus, C-terminus, and loop 9 indicated, (b) sfGFP-Car9 and (c) sfGFP::Car9. Car9 is depicted as a blue ball.

Surface plasmon resonance (SPR) analysis of the molecular mechanisms through which Car9 binds to silica surfaces at pH 7.5 indicates that sfGFP-Car9 exhibits a sigmoidal adsorption behavior typical of a cooperative process.[15] By contrast, the sfGFP-K8AK11A mutant binds to silica in a Langmuir-like fashion and with lower rate constants and saturation coverage relative to sfGFP-Car9, implicating persistent contacts of a cluster of basic residues with the surface as essential for high-affinity cooperative binding (Hellner et al., manuscript in revision).

In addition, it has been found by SPR that sfGFP-Car9 exhibit lower affinity for silica under basic conditions and that fusion of the Car9 sequence to the N-terminus of sfGFP or within loop 9 reduces silica-binding affinity (Hellner et al., unpublished). In brief, the composition of the Car9 variant, the insertion point on the host protein framework, and the environmental condition all influence silica binding.

Based on this understanding, we built bifunctional sfGFP derivatives containing two Car9 derivatives with the aim of controlling the assembly/disassembly of silica nanoparticles (NPs) under different solution conditions.

1.2. Silica Nanoparticle Chemistry and Protein Adsorption

Silica is an abundant material that has been widely used as a separation media, catalyst support, and for the formulation of cosmetics, biomedical materials and pharmaceuticals due to its nontoxicity and biocompatibility.[16, 17] Colloidal systems of silica particles interact through attractive Van der Waals and repulsive electrical double layer forces, as predicted by Derjaguin, Landau, Verwey, and Overbeek (DLVO) theory.[18, 19] The negative electrical charge on silica surface originates from the pH-dependent deprotonation of silanol groups which can exist as isolated silanols (≡Si−OH), geminal silanols (=Si(OH)$_2$), or vicinal silanols (H-bonded silanols) at abundances that are influenced by the synthesis method.[20] Consistent with the basic Stern model, silica particles carry no charge at low pH (~2-4) and have a decreasing surface charge with the increasing pH in negative and ionic strength.[21] Salt is known to weaken the double layers and caused instability and aggregation, and a critical coagulation concentration (CCC) is suggested to separate the regimes of slow and fast aggregation. CCC is minimum concentration of an inert eletrolyte which strongly depends on the valency of the counterions, but is also influenced by concentration and nature of nanoparticles.[18] It is predicted that the suspension becomes more stable at higher surface ionization and decreasing salt level based on the decrease in the aggregation rate constant and electrophoretic mobility.[21]

Over the years, the kinetics and fundamentals of protein adsorption on flat surfaces (including silica) have been studied with surface-sensitive spectroscopic techniques,[22, 23] ellipsometry or reflectometry.[24, 25] However, a significant gap remains in our understanding of protein adsorption onto nanoparticles due to the complexity introduced by high surface curvature.[26] Previous work from the Perry group has revealed that the adsorption of certain silica-binding peptide to silica nanoparticles was driven by multiple interactions, including electrostatic interaction, hydrophobic interactions, hydrogen bonding, as well as ion-dipole, dipole-dipole, and van der Waals interactions[10, 27-30]. A multilayer was suggested to form in the adsorption process, in which prevailing interactions are determined by the identity of the peptide, the substrate's surface functionality, the peptide bulk concentration and the solution bulk pH.[10, 27] Both an increase in particle size and in pH led to an increase amount of bound peptide, as a result of increased surface ionization.[30] Bharti *et al.* who studied the nonspecific interaction of silica nanoparticles with Lysozyme found that the protein-induced particle aggregation by bridging exhibited different structures as a function of pH.[31] Bridging attraction and heteroaggregation of silica nanoparticles was also observed in the presence of polyethylene oxide and thermoresponsive polymer chains.[32, 33]

1.3. Colloidal Self-assembly

Colloidal particles range from nanoscale to microscale. Their self-assembly has been well studied and many different methods can be used to achieve it. Compared to standard top-down fabrication methods, such as optical lithography, colloidal self-assembly provides easier fabrication schemes and the possibility of manipulating assembly at the nano- and microscale, especially in three dimensions.[34] Commonly used approaches include spontaneous colloidal crystallization, guided assembly on patterned substrates,[35, 36] assembly in emulsions or driven by light or magnetic fields,[37-39] and connecting particles through the use of linkers. For the latter, nucleic acids have been widely used to form large structures of particles while polymers have been popular to mediate aggregation at different temperatures.[40, 41] Nevertheless, conducting particle assembly with these methods can be limited by the number of available interactions and the length scales.[34]

In this project, we used solid binding proteins to drive the assembly of nanoparticles to access a much larger chemical and structural design space.

1.4. Förster Resonance Energy Transfer

Förster resonance energy transfer (FRET) occurs between two chromophores in close proximity through non-radiative dipole-dipole interaction when a donor chromophore is excited in the presence of an acceptor chromophore.[42] Three requirements must be met for molecules to generate a FRET signal: (i) the emission spectrum of the donor must overlap with the absorption spectrum of the acceptor; (ii) the distance separating the two fluorophores must be inferior to 10 nm (100 Å); and (iii) a long-range dipole-dipole interaction must exist between the donor and acceptor.[42, 43] The FRET efficiency, defined as the quantum yield of the process, can be measured through the donor fluorescence intensity, the donor lifetime in the excited stage, the acceptor emission intensity and the donor/ratio intensity ratio (also known as ratiometric FRET).[44] Most commonly, the FRET efficiency is determined by measuring the change of the donor fluorescence intensity in the absence and presence of acceptor, and calculated using:

$$\mathrm{E} = 1 - \frac{I_{DA}}{I_D} \qquad \text{(I)}$$

where I_{DA} and I_D are the total donor fluorescence intensities in presence and absence of acceptor respectively. The FRET efficiency is inversely proportional to the sixth power of the distance between donor and acceptor and this distance can be obtained from Förster's conversion formulae:

$$\mathrm{R} = R_0 \sqrt[6]{\frac{1-E}{E}} \qquad \text{(II)}$$

Where R_0 is the characteristic distance at which the FRET efficiency is 50%. This value depends on the identity of the chromophore pairs and it can be calculated using:

$$R_0 = 9.78 \times 10^3 [\kappa^2 n^{-4} Q_D J(\lambda)]^{1/6} \text{ (in Å)} \quad \text{(III)}$$

Where κ^2 is the orientation factor between donor and acceptor; n is the refractive index of the medium; Q_D is the quantum yield of the donor in the absence of the acceptor; and J(λ) is the degree of spectral overlap between the donor emission spectrum and the acceptor absorbance spectrum. The orientation factor κ2, which describes the relative orientation of the donor and acceptor transition dipoles ranges from 0 to 4, and is usually assumed to be equal to 2/3.[45]

Determining the precise location between specific molecules is of major interest in many areas of biological research, such as nucleic acid hybridization,[46] biological membrane mapping and protein studies.[47, 48] Non-radiative energy transfer is not sensitive to the surrounding solvent shell, therefore it gives unique molecular information.[49] Although it remains affected by cross-talk and limitation for donor:acceptor stoichiometry, [44] FRET has been widely used as a molecular ruler to probe distances between specific sites and to gain insights into the structure and molecular interactions of macromolecules.[50] Many naturally existing and synthetic materials can be used as a FRET pairs. These include organic dyes (FITC, Rhodamine, Alexa-dyes, etc.), inorganic ions (e.g. Eu^{3+}, Tb^{3+}, Yb^3+), fluorescent proteins (FP) such as CFP (cyan), YFP (yellow) and GFP (green), and quantum dots (QDs) which are fluorescent semiconductor nanocrystals.[51] Significant progress has been achieved by using GFP mutants to monitor cellular physiology via FRET due to its intrinsic ability to generate fluorescence in live tissues.[52] The preferred CFP-YFP pair have a significant spectral overlap and are routinely use to detect molecular conformation changes and to monitor the cellular concentration of free calcium ions.[53]

Here, we use FRET to study the proximity of sfGFP-Car9 variants to silica nanoparticles that encapsulate the organic dye Rhodamine (RhSiNP). Although the overlap in the spectra of sfGFP and RhSiNP is not extensive (Figure A1), we hypothesized that FRET would still occur between the two chromophores, allowing us to how study the influence of solid binding protein identity and solution conditions (pH, salt concentration), on silica binding, and colloidal aggregation and disaggregation. We complement these studies with dynamic light scattering (DLS) measurements, pull-down assays and scanning electron microscopy (SEM) imaging to gain insights on the molecular mechanisms through which various Car9 fusion proteins bind to silica and build a stimuli-responsive protein-nanoparticles system that exhibits controllable assembly/disassembly behavior.

2. MATERIALS AND METHODS

2.1. DNA Manipulations and Proteins Expression and Purification

Superfolder GFP (sfGFP) was modified with wild type and mutant Car9 sequences using standard molecular biology approaches. These segments were genetically fused to the C-terminus of the protein through a GGGS linker to yield sfGFP-X constructs, inserted within loop 9 of the protein to yield sfGFP::X constructs, or inserted at both locations to yield sfGFP::X-X constructs.[14] The following mutants were used in this study, wild type sfGFP, sfGFP-Car9, sfGFP::Car9, sfGFP-K8AK11A, sfGFP::Car9-Car9 and sfGFP::Car9-K8AK11A. All proteins were expressed in *E. coli* BL21(DE3) cells. With sfGFP, sfGFP-Car9, sfGFP::Car9, sfGFP::Car9-Car9 already available from previous work (Hellner et al., unpublished),[15] we only constructed sfGFP::Car9-K8AK11A. To this end, we made use of pET-24a(+)-sfGFP::Car9 which encodes the sfGFP::Car9 fusion between *Nde*I and *BsrG*I restriction sites with a Car9 segment flanked by *BamH*I and *Spe*I sites, and plasmid pET-24a(+)-sfGFP-K8AK11A which contains the K8AK11A Car9 variant between *Hind*III and *Xho*I sites. Plasmid pET-24a(+)sfGFP::Car9-K8AK11A was thus built by inserting the *Nde*I-*BsrG*I DNA fragment encoding sfGFP::Car9 into the same sites of pET-24a(+)-sfGFP-K8AK11A.

BL21(DE3) cells harboring appropriate plasmids were grown overnight at 37 ℃ in 25 mL Luria broth (LB) medium supplemented with 50 μg/mL kanamycin. Aliquots (10 mL) were used to inoculate 500 mL of LB medium supplemented with 50 μg/mL kanamycin. Cultures were grown at 37°C and recombinant protein production induced with 1 mM isopropyl β-D-thiogalactopyranoside (IPTG) in mid-exponential phase (A_{600}=0.4-0.6, about 1.25-1.75 h after inoculation). Cells were grown for an additional 3.5-4 h to accumulate recombinant proteins. Cultures were centrifuged at 4,000 *g* for 10 min, resuspended in 35 mL of 20 mM Tris-HCl, 2 mM EDTA, 1 mM PMSF, pH 7.5, and lysed by 6 consecutive cycles of sonication on a Branson sonifier operated at 30% duty cycle. Samples were centrifuged for 15 min at 10,000 *g* to sediment insoluble material, and clarified extracts were subjected to a 15 min heat shock at 70°C to precipitate thermolabile proteins. A second cycle of centrifugation at 10,000 g for 15 min was used to remove aggregated material.[11] A 5mL DEAE Cartridge column was used for the purification of wild type sfGFP through fast-protein liquid chromatography (FPLC) using 20 mM Tris-HCl, pH 7.5 as a load and wash buffer and 20 mM Tris-HCl, 1M NaCl, pH 8 as the elution buffer. Elution was performed at 2 mL/min using a linear gradient (from 0 to 1M NaCl). Successive 2mL fractions were collected based on A_{280}. For Car9 fusion proteins, clarified and heat-shocked samples were subjected to silica affinity chromatography using 6 g of Davisil silica (Sigma Aldrich, 15 nm pore size, 35-70 nm particle size) that had been washed three times in 20 mM Tris-HCl at pH 7.5. Excess target protein and contaminants were removed by aspiring 100 mL of buffer through the silica matrix. Proteins were eluted in 30 mL of buffer supplemented with 0.5 M Lysine at pH 8.25.[9] All proteins were analyzed by SDS-PAGE to assess purity and identity. The buffer was exchanged to 20 mM Tris-HCl at pH 7.5 using 10,000 MWCO SnakeSkin Dialysis tubing. The concentration of each sample was determined using the bicinchoninic acid (BCA) assay after 30 min of incubation at 37 ℃.

2.2. Protein-silica Nanoparticles Assembly and Disassembly Experiments

The nanoparticles used in the study are Rhodamine-encapsulated silica nanoparticles (RhSiNP) (Micromod Partikeltechnologie GmbH, Germany, 40 μM stock solution) with a manufacturer-specified diameter of 10 nm and a hydrodynamic diameter of 15 nm (Figure A3). The particles exhibit red fluorescence at 582 nm when excited at 554 nm (Figure A1). Different sfGFP derivatives were mixed with RhSiNP nanoparticles at a final concentration of 5 μM for proteins and 1 μM for RhSiNP in 20 mM Tris-HCl, pH 7.5 by pipetting. For each protein candidate, two 15 mL conical bottom tubes supplemented with 2.5 mL of the mixture were incubated on a rotary mixer for 30 min at room temperature. A 400 µL aliquot of sample from tube 1 was used for FRET, DLS and fluorescence assay experiments, which are described in detail below. Approximately 25 µL of 1M NaOH was added to tube 2 to raise the sample pH to 8.5 as determined using a pH meter. After another 30 min of incubation, aliquots from tube 2 were analyzed as above. For protein sfGFP::Car9-Car9 and sfGFP::Car9-K8AK11A, five additional tubes containing 2.5 mL of mixture were prepared for pH cycling experiments. To lower the pH back to 7.5, approximately 25 µL of a 1M HCl solution was added a NaOH-treated sample.

To investigate the influence of salt, solutions of 20 mM Tris-HCl, pH 7.5 were supplemented with 12.5, 25, 50 or 100 mM NaCl. Protein sfGFP::Car9-Car9 at 5 µM was mixed with RhSiNP at 1 μM, and size distribution and ζ-potential were measured after 30 min incubation at room temperature. DLS experiments were also conducted with nanoparticles and either sfGFP::Car9-Car9 or sfGFP::Car9-K8AK11A (1:5 NP:protein rartio) in 20 mM Tris buffer supplemented with

100 mM NaCl at both pH. Control experiments were done with pure RhSiNP in pH 7.5 and 8.5 buffer supplemented or not with 100 mM NaCl.

FRET experiments **-** Fluorescence intensity measurements were collected on a F-4500 fluorescence spectrophotometer (Hitachi, Japan) in wavelength scan mode from 450-650 nm with a $\lambda_{ex}$of 485 nm, slit widths set at 2.5 nm, and at a scan speed of 240 nm/min. Samples (400 µL) were aliquoted in a 10 mm path length quartz cuvette that had been washed with deionized water and ethanol and air dried before use. Control experiments were conducted with pure protein and with nanoparticles diluted to 5 µm and 1µm, respectively with 20 mM Tris-HCl buffered at pH 7.5 or 8.5. Fluorescence spectra of protein solutions (donor) diluted in 20 mM Tris-HCl buffered at pH 7.5 or 8.5 were also collected in the absence of acceptor (particles). = Fluorescence spectra of RhSiNP in 20 mM Tris-HCl with the same concentration as in each pH cycling buffered at pH 7.5 or 8.5 were collected with excitation at 485 nm.

Size Distribution and Zeta Potential measurements - DLS measurements were used to determine size distribution and zeta (ζ) potential of colloidal suspensions using a Zetasizer Nano ZS (Malvern Instruments, U.K.) operated with a 4 mW HeNe laser at 633 nm and a backscatter positioned at 173° for the detection of scattered light. Each sample (400 µL) was placed in a disposable polystyrene cuvette and allowed to sit in the instrument for 120 s at 25 ℃ before being measured three times. The number of runs for each measurement was automatically controlled by the program. Size distributions were extracted from intensity measurements. The ζ-potentials were obtained from the electrophoretic mobility (μ_e) using the Henry Equation and 1 mL of sample in a folded capillary cell. DLS measurement for solutions of pure RhSiNP (1 µM) and protein (5 µM) were also performed at both pHs.

SEM imaging - Scanning Electron Microscopy (SEM) images were acquired on a Sirion-XL30 instrument (FEI). Samples were diluted 50-fold with deionized water and a 15 µL aliquot was deposited on a 5 x 5 mm silicon chip cut from a wafer. The sample was air dried overnight in a disposable plate with cover. Through-Lens detection (TLD) was used for SEM imaging at 10kV and spot number 3. Images were processed using the ImageJ software.

Fluorescence assays - After 30 min of incubation, 500 µL samples were taken into 1 mL centrifuge tubes by pipetting and subjected to 15 min of centrifugation at 14,000 rpm (16,873 g). Aliquots (125 µL) of supernatants were dispensed in triplicate into the wells of a 96-well microplate and fluorescence intensity was measured at 510 nm on a SpectraMax M5 instrument (Molecular Devices) using an excitation wavelength of 485 nm and an auto cutoff setting of 495 nm. Each reading was repeated 30 times to minimize variability. The fluorescence of pure protein solutions at 5 µM following centrifugation were measured on the same plate to serve as a control.

3. RESULTS AND DISCUSSIONS

3.1. Binding of Silica Nanoparticles by Single-tag sfGFP Derivatives

The normalized absorption and emission spectra of sfGFP and RhSiNP are shown in Figure A1 (Appendix). An overlap was observed between the adsorption spectrum of sfGFP (donor) and the emission spectrum of RhSiNP (acceptor), indicating suitability for FRET analysis. Because the presence of a Car9 tag within loop 9 or at the C-terminus of sfGFP does not change the fluorescence spectra,[14] all sfGFP variants studied here should have similar FRET properties. According to the manufacturer, the surface of RhSiNP is terminated with silanols and the rhodamine dye is evenly encapsulated within particles. We first measured the fluorescence of pure RhSiNP at 1µM and that of sfGFP at 5 µM in Tri-HCl, pH 7.5 upon excitation at 485 nm. sfGFP

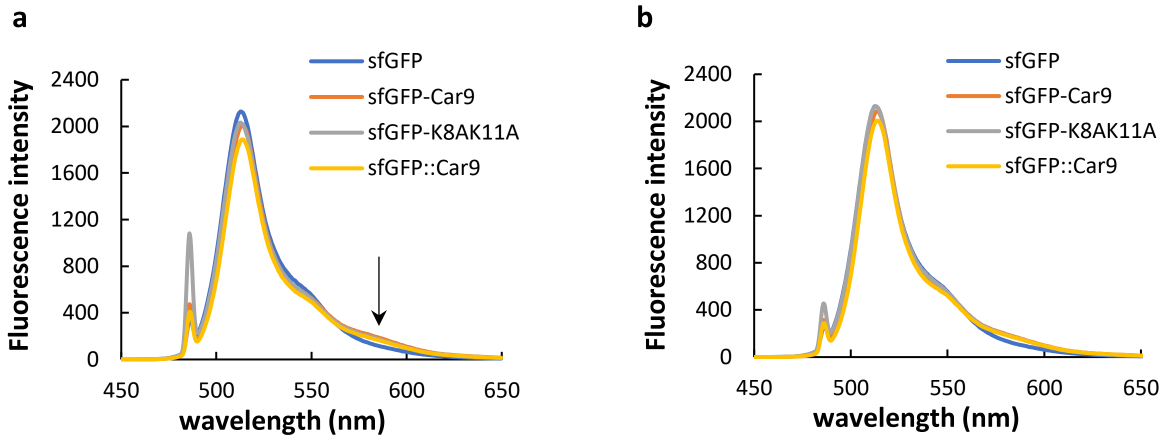

Figure 2. Fluorescence spectra of protein-RhSiNP mixtures for WT sfGFP and single Car9-tagged sfGFP variants excited at 485 nm in buffers held at pH 7.5 (a) or pH 8.5 (b). The arrow identifies the rhodamine B emission peak (~580 nm) that appears as a result of FRET.

emitted strong fluorescence at 512 nm and RhSiNP only exhibited a faint peak at 582 nm (Figure A2 in the Appendix), ruling out the possibility of cross talk for this FRET pair.

Protein were next mixed with RhSiNP at a molar ratio of 5:1. This ratio was determined by an optimization process that is described below. Fluorescence spectra of WT sfGFP and single-tagged sfGFP derivatives following excitation at λ_{ex}=485 nm are shown in Figure 2. Apart from WT sfGFP which has little affinity for silica and serves as a control, all spectra contained a small peak centered at ~580 nm and corresponding to the emission of Rhodamine. Thus, energy transfer occurs between proteins and RhSiNP. The calculated FRET efficiencies (Table 1) show that sfGFP::Car9 exhibits the highest FRET value among all single-tagged variants studied. This can be explained by a closer proximity (Table 1) of the sfGFP chromophore to encapsulated rhodamine molecules when Car9 is positioned in the loop rather than being fused to the C-terminus of sfGFP. However, the increase in FRET could also be due to the higher affinity of sfGFP::Car9 for RhSiNP as donor-acceptor concentration influences FRET efficiency.[54] Yet, SPR experiments indicate that sfGFP-Car9 has higher affinity for silica surfaces than sfGFP::Car9 (Hellner et al. unpublished).

Because these experiments were conducted on silica-coated SPR chips we sought to determine if curvature might also influence binding. We therefore performed pull-down experiments in which proteins were mixed with RhSiNP at a 5:1 molar ratio, samples were subjected to a high-speed centrifugation step, and the fluorescence of (presumably free) proteins remaining in the supernatants was measured. Figure 3 shows that there was a ~11% decrease in the fluorescence of supernatants recovered from sfGFP::Car9 mixtures compared to sfGFP-Car9 mixtures at pH 7.5 On the other hand, and consistent with the weaker affinity of sfGFP-K8AK11A for silica as measured by SPR (Hellner et al., manuscript in revision), and with the FRET data of Table 1, about 5% more sfGFP-K8AK11A remained in solution compared to sfGFP-Car9. This behavior was accentuated at pH 8.5 where silica affinity is reduced. While these results suggest that sfGFP::Car9 may have a slightly higher affinity for silica nanoparticles relative to sfGFP-Car9, additional experiments will be needed to determine if protein-decorated RhSiNP are indeed removed by centrifugation or if the results of Figure 3 only reflect the sedimentation of small aggregates. At present, the most likely explanation for the increase in FRET signal observed with sfGFP::Car9 is related to chromophore position effects, while the decrease associated with a shift to pH 8.5 is related to affinity effects.

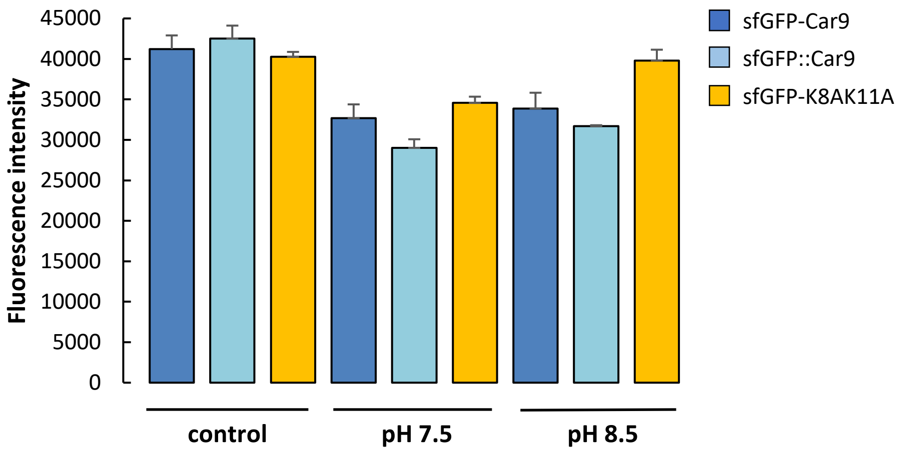

Figure 3. Fluorescence of the supernatant from pure protein (control), protein-RhSiNP system with sfGFP-Car9, sfGFP::Car9 and sfGFP-K8AK11A at pH 7.5 and 8.5.

Table 1. FRET efficiency and donor-acceptor distance r of protein-RhSiNP system

FRET efficiency[a]	pH 7.5	pH 8.5	% of decrease	r @ pH 7.5[b]	r @ pH 8.5
sfGFP	0.034	0.031	8.80%	9.61	9.76
sfGFP-Car9	0.092	0.065	29.30%	8.06	8.58
sfGFP-K8AK11A	0.077	0.036	53.20%	8.32	9.51
sfGFP::Car9	0.147	0.102	30.60%	7.37	7.90
sfGFP::Car9-Car9	0.286	0.111	61.20%	6.41	7.78
sfGFP::Car9-K8AK11A	0.227	0.111	51.10%	6.75	7.78

[a] pH was shifted only once from 7.5 to 8.5 for WT sfGFP and single Car9-tagged derivatives. Multiple cycles of pH shifts were performed for dual-tagged sfGFP derivatives but the efficiency shown in the table was calculated from the first shift.

[b] Calculated by using formula (II). Assume the R_0 is the same for each protein and equals to 5.5 nm.[56, 57]

3.2. Silica Binding by Dual-tagged sfGFP Derivatives

We next measured intermolecular FRET between RhSiNP and bifunctional sfGFP derivatives bearing the Car9 SBP within loop 9 and either a WT Car9 extension (sfGFP::Car9-Car9) or its K8AK11A variant (sfGFP::Car9-K8AK11A) at their C-termini. Table 1 shows that at pH 7.5, FRET efficiencies were 3-fold higher with sfGFP::Car9-Car9 relative to sfGFP-Car9. A similar 3-fold increase was observed when sfGFP::Car9-K8AK11A was used in place of sfGFP-K8AK11A. Remarkably, a shift to pH 8.5 reduced FRET to 0.111 in both cases, a value that is only ~10% higher than that of the sfGFP::Car9-RhSiNP pair at the same pH (Table 1). Taken together, these results suggest that: (1) bifunctional variants increase FRET by bridging RhSiNP particles and allowing contributions from multiple acceptors; (2) a C-terminally located K8AK11A variant of Car9 is less efficient than the wild type SBP in promoting such bridging; (3) the major contributor to the FRET signal are brought about when the loop-inserted Car9 SBP bring the sfGFP chromophore close to the nanoparticles; and (4) higher pH weaken the bridging interactions and leads to dissociation.

To test these hypotheses, we performed DLS measurement of size distribution using a 5:1 molar ratio of protein to RhSiNP particles. This ratio was selected through an optimization campaign starting at 1:1 and progressively increasing the concentration of sfGFP::Car9-Car9 to achieve nearly quantitative depletion of the protein in solution at pH 7.5 (Figure 6).

Untreated RhSiNP have a hydrodynamic diameter (D_h) of ~15 nm at both pH 7.5 and 8.5 (Figure A3) but form large aggregates (~825 nm) within 30 min of sfGFP::Car9-Car9 addition, and there is a complete depletion of free particles (Figure 5a). Strikingly, a shift in pH to 8.5 completely resolves the aggregates into species whose D_h (24 nm) is consistent with that of single RhSiNP coated with a protein shell (the β-barrel of sfGFP is approximately 4 nm in height) (Figure

5a). Interestingly, the dissociated species could be re-aggregated into ~1100 nm clusters by returning the solution to pH 7.5 (Figure 5a).

To further investigate the reversibility of the aggregation/disaggregation process, we subjected samples to multiple pH cycles and calculated FRET at the conclusion of each step. Figure 7 shows that the system exhibited a convincing cyclic behavior as early as in the second cycle of pH change. These data suggest are fully consistent with a reversible RhSiNP assembly/disassembly enabled by bifunctional solid binding proteins and driven by changing the solution conditions by a single-unit of pH.

Pull down experiments conducted with at a 5:1 molar ratio of sfGFP::Car9-K8AK11A to RhSiNP revealed that aggregates were also formed and could be removed by centrifugation. However, and consistent with the weaker affinity of K8AK11A for silica, some of the protein remained in solution (either as free species or as small aggregates that were too small to undergo sedimentation under our experimental conditions) (Figure 6). The system also exhibited a pH-mediated association-dissociation behavior (Figure 6) except that the aggregates formed at pH 7.5 corresponded to a broader distribution of species with a smaller mean hydrodynamic diameter (D_h ~160 nm) (Figure 5b). This results is consistent with the lower affinity of K8AK11A for silica: a smaller aggregate size should be expected when all the high-affinity ::Car9 bonds have been formed and the clusters are terminated with a protein corona exposing a weaker binder (K8AK11A) to the solvent that cannot effectively bridge additional particles. Disaggregation / re-aggregation behavior was also observed by DLS and FRET (Figure 5b and 7b) with the expected weaker FRET efficiency and an apparent resolution of aggregates into a size (D_h ~120 nm) that balances protein bridging effects and hydrodynamic forces. In short, aggregate size can be tuned by choosing an SBP with lower affinity for silica.

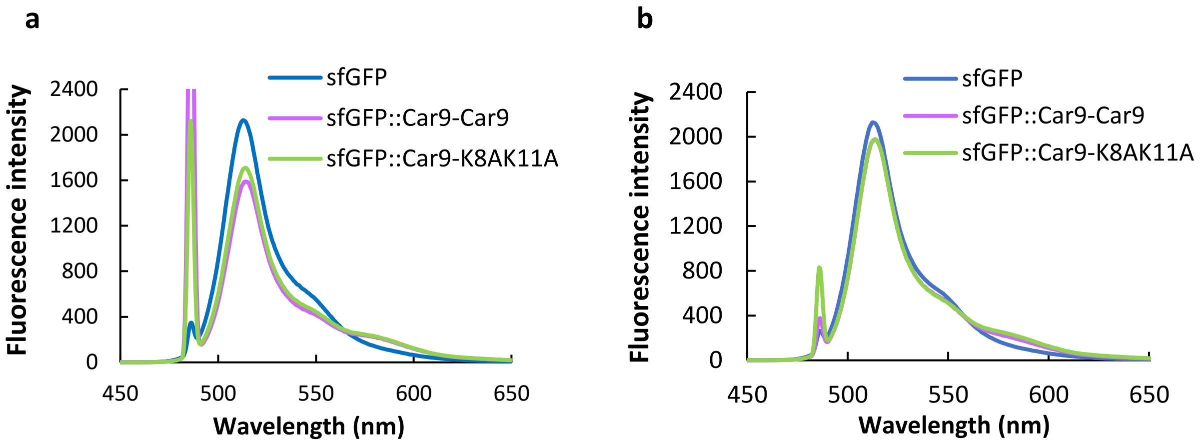

Figure 4. Fluorescence spectra of protein-RhSiNP system with dual-tagged sfGFP derivatives at λ_{ex}=485 nm for pH (a) 7.5 and (b) 8.5

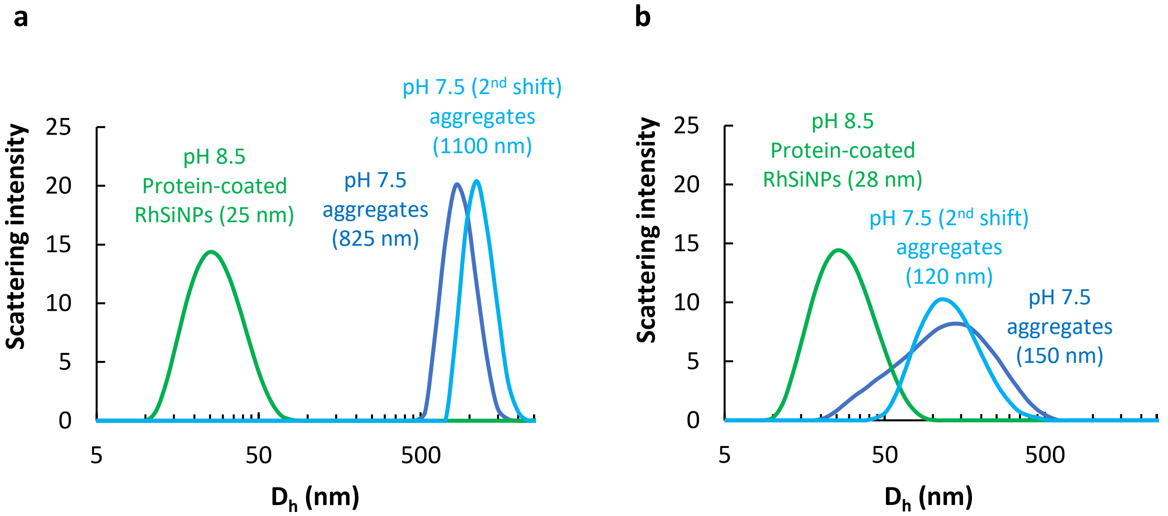

Figure 5. Size distribution of protein-RhSiNP system with (a) sfGFP::Car9-Car9 and (b) sfGFP::Car9-K8AK11A for two pH shifts

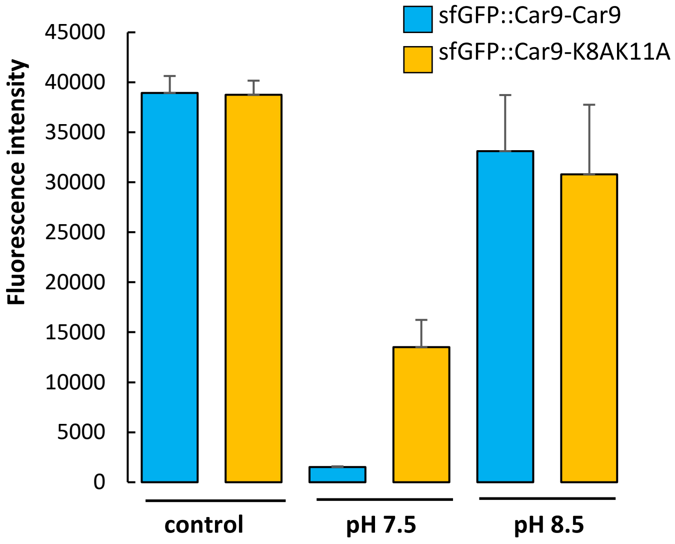

Figure 6. Fluorescence of the supernatant from pure protein and protein-RhSiNP system with sfGFP::Car9-Car9 and sfGFP::Car9-K8AK11A at pH 7.5 and 8.5.

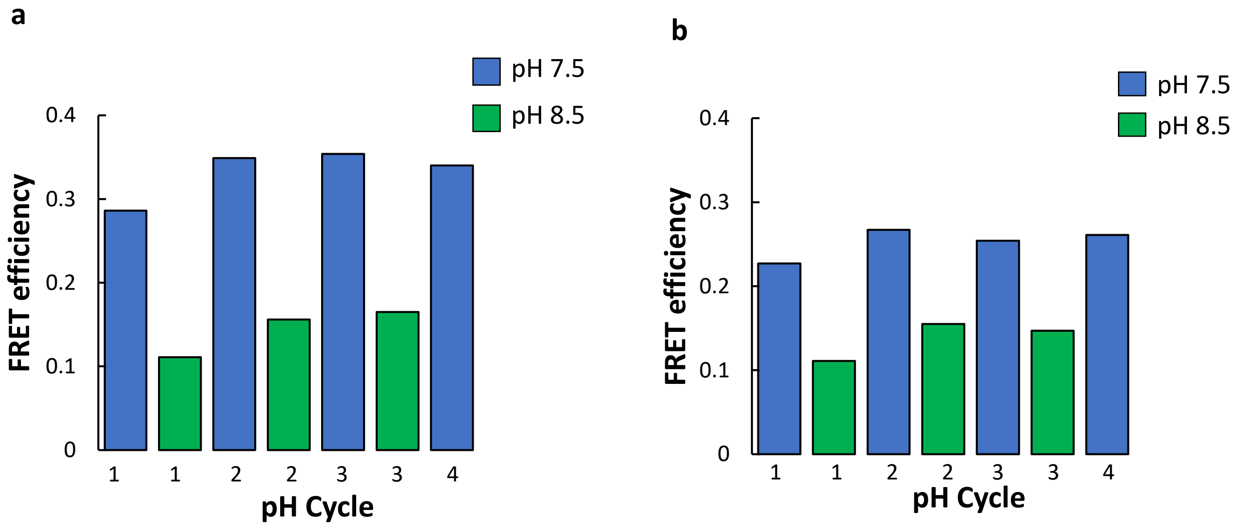

Figure 7. FRET efficiency of sfGFP::Car9-Car9 -RhSiNP (a) and sfGFP::Car9-K8AK11A-RhSiNP samples (b) subjected to successive pH cycles. All experiments were conducted in 20 mM Tris-HCl with 5 µM of protein and 1 µM of particles as described in Materials and Methods.

SEM images of RhSiNP mixed with sfGFP::Car9-Car9 or sfGFP::Car9-K8AK11A at pH 7.5 and 8.5 are shown in Figure 8. As expected from DLS data, we observed larger aggregates with the former protein (Figure 8a-c), and efficient resolution into individual particles and small clusters under basic condition (Figure 8b-d).

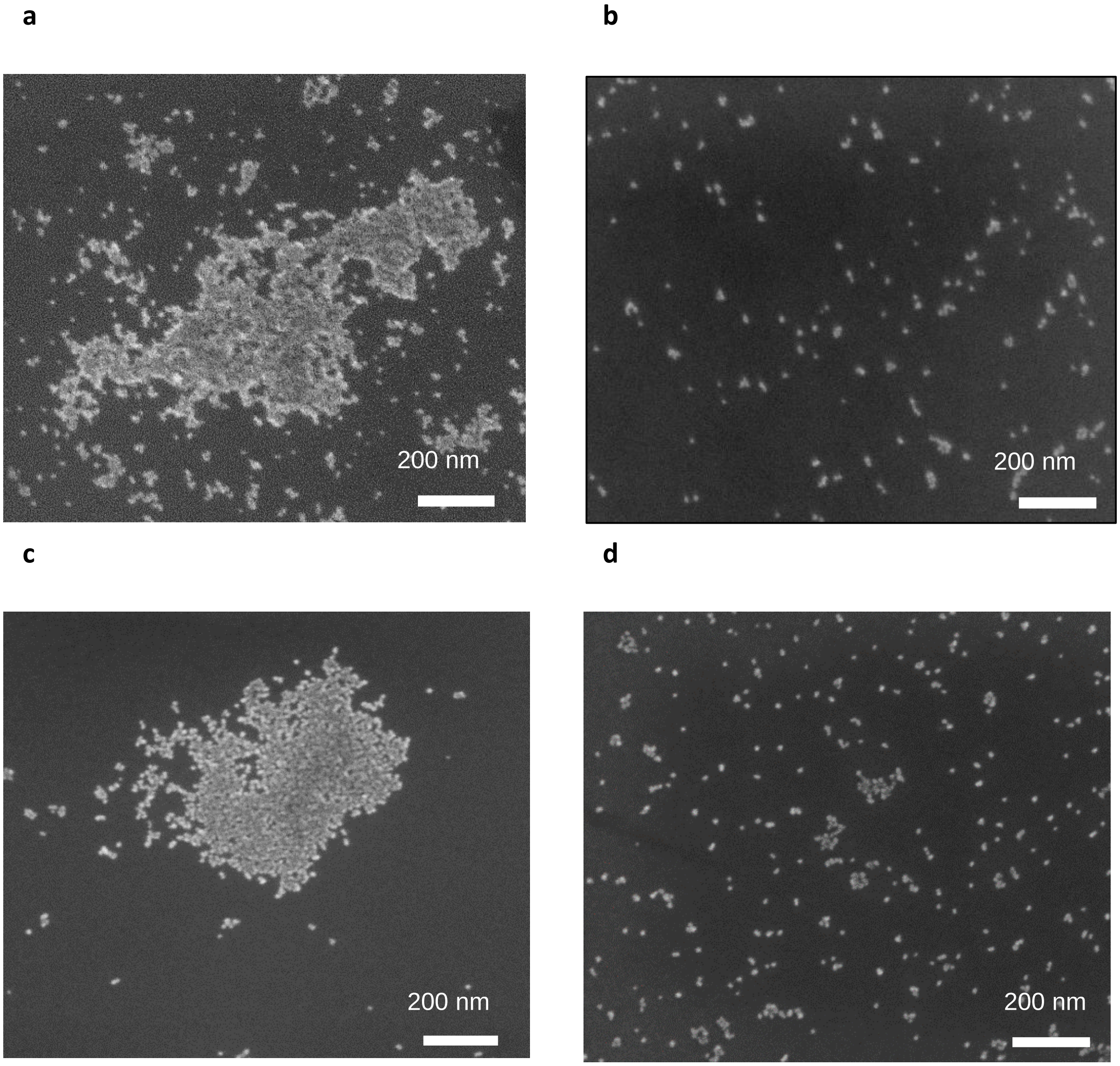

Figure 8. SEM image for RhSiNP (1 µM) aggregates and resolved clusters obtained with 5 µM sfGFP::Car9-Car9 at pH (a) 7.5 and (b) 8.5, and 5 µM sfGFP::Car9-K8AK11A at pH (c) 7.5 and (d) 8.5

3.3. Influence of NaCl

To gain insights on the role of electrostatics, we conducted additional experiments with the sfGFP::Car9-Car9-RhSiNP system, increasing the NaCl concentration from 0 mM to 100 mM at pH 7.5. Figure 9 shows that this operation led to a progressive increase in aggregate size (from ~825 to ~1700 nm (Figure 9a). Mean aggregate sizes at and full width at half max values are shown in Table A1. Not unexpectedly, the particles' ζ potential decreased with increasing NaCl concentration as would be expected from the formation of a neutralizing double layer[21](Figure 9b). Based on DLVO theory, the repulsive force from the double layer will be weakened by strong ionic strength counterions which should favor protein-induced coagulation. Control experiments performed in the presence of 100 mM NaCl but in the absence of protein shows that while there was a small amount of aggregation, most particles remain soluble at both pH 7.5 and 8.5 (Figure A4). (The smaller aggregates seen at pH 8.5 may be due to a higher level of surface ionization.)[21] Thus, sfGFP::Car-Car9 is responsible for driving aggregate formation and can do so more easily as some of the surface charges are screened.

To determine if aggregates formed in the presence of salt could be resolved we collected DLS spectra for both sfGFP::Car9-Car9 and sfGFP::Car9-K8AK11A after switching the pH to 8.5. In the case of sfGFP::Car9-Car9, aggregates did not completely break down into single particles, and most remained as large (~615 nm) aggregates with a small amount of individual protein-coated particles (~25 nm) and small clusters (-45 nm) (Figure 10a). However, by using sfGFP::Car9-K8AK11A which forms ~1500 nm aggregates at pH 7.5, we were able to achieve quantitative disassembly into individual protein-coated NPs (Figure 10b). The supposed that the higher salt concentration stabilized the aggregate size in the disassembly process, but apparently this is more prominent to WT Car9 than K8AK11A mutant. This likely reflects both the different binding modalities of Car9 and K8AK11A for silica (Hellner et al, unpublished), and the lower affinity of K8AK11A for silica in the presence of NaCl. Clearly though, aggregate size and disaggregation efficiency can be tuned by selecting appropriate bifunctional proteins and solution conditions.

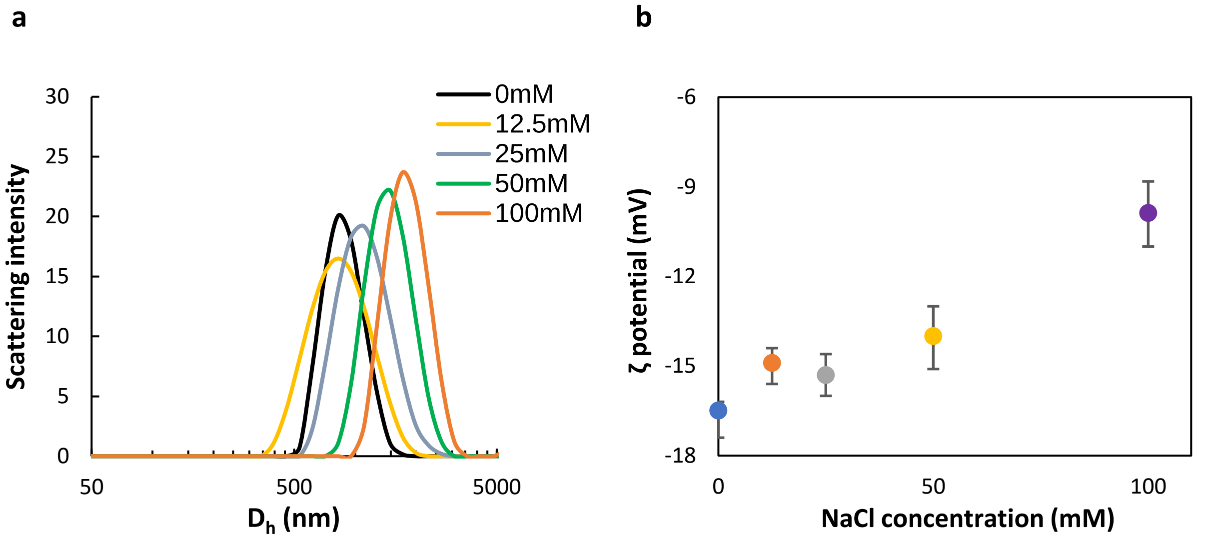

Figure 9. (a) Size distribution and (b) ζ potential for the sfGFP::Car9-Car9 -RhSiNP system in 20 mM Tris-HCl, pH 7.5 in the presence of the indicated concentrations of NaCl.

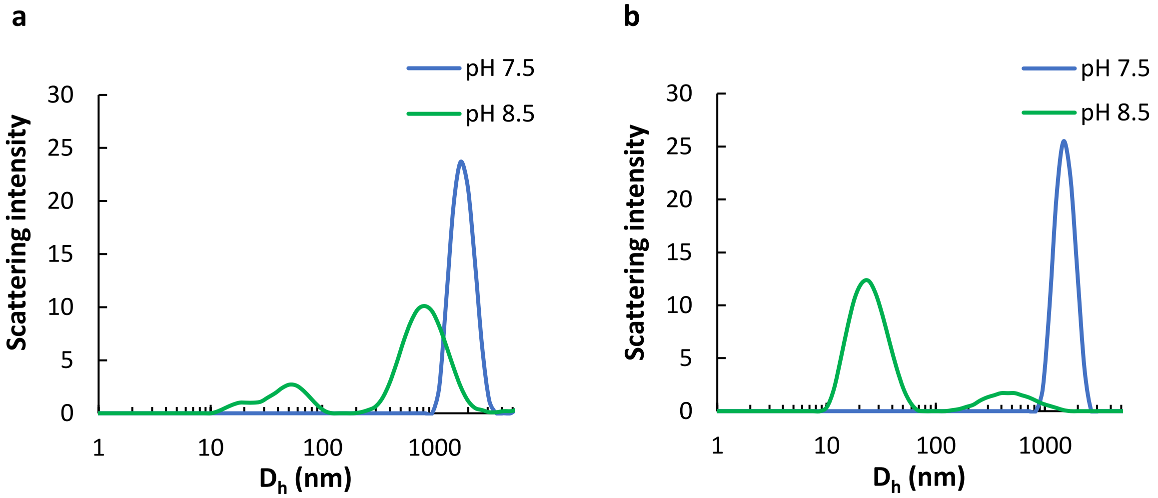

Figure 10. Size distribution of protein-RhSiNP system with (a) sfGFP::Car9-Car9 and (b) sfGFP::K8AK11A in Tirs-HCl with100mM NaCl at pH 7.5 and pH 8.5

4. CONCLUSION

Motivated by the challenge of controlling the assembly of nanoscale materials in a precise and flexible fashion, this study focused on using bifunctional solid binding proteins tagged with the Car9 silica binding peptide to build a dynamic protein-nanoparticle system in which assembly - disassembly behavior can be controlled by changing solution condition (e.g pH and salt concentration). Interactions between Car9 and the silica interface are dominated by electrostatic interactions between the positively charged lysine and arginine residues in Car9 and the negatively charged silanol groups on the silica surface. With SPR data showing differential binding of Car9 variants fused in different locations of the sfGFP framework depending on the solution pH, we intend to further explore the use of Car9-tagged proteins as molecular linkers to assemble and disassemble silica nanoparticles.

FRET was utilized here to examine the separation and orientation of Car9 fusion proteins and RhSiNP, and gain insights on the nature of binding process. While sfGFP and Rhodamine are not an ideal FRET pair given the small overlapping area in their spectra compared to popular FRET materials such as CFP and YFP, we have shown here that this donor-acceptor pair is very valuable to capture the binding behavior of Car9 variants as a function of solution pH. It should be broadly useful in the future to study protein-mediated assembly of NPs.

DLS measurements which are based on how the intensity of scattered light correlate to particle size and distribution have confirmed the aggregation and disaggregation of RhSiNP in solutions held at pH 7.5 and 8.5, respectively. Aggregates had a larger size (~825 nm) when formed with sfGFP::Car9-Car9, and a smaller size (~150 nm) when sfGFP::Car9-K8AK11A was used. This difference in size is related to the differential ability of WT Car9 and K8AK11A to bind silica, and provide a “handle” for the construction of a size-tunable system. Both clusters can decompose into single protein-coated RhSiNPs by a simple shift of one pH unit and the process shows good reversibility.

Control of assembly could also be achieved by changing the salt concentration. Although larger aggregates are obtained with both dual-tagged proteins, they can be disassembled with sfGFP::Car9-K8AK11A system while clusters of intermediate sizes are obtained with of sfGFP::Car9-Car9. This provides an additional handle to tune aggregate size and to assemble particles at the same solution pH by changing NaCl concentration. We also observed an increase in aggregate size with the NaCl concentration, and additional work will be needed to test our hypothesis that a complex interplay between SBP composition and binding modality, silica surface chemistry and double layer structure ultimately control aggregate size.

By synthesizing solid binding proteins incorporating two SBPs with different binding behavior, we have developed a novel approach to manipulate the aggregation and disaggregation of silica nanoparticles using changes in solution acidity. We have further shown that aggregate size is tunable by changing SBP composition and salt concentration. Achieving dynamic control of nanoparticle assembly with computationally designed proteins is the next frontier for the predictive production of hierarchical architectures useful in biomedicine, biomaterial fabrication and energy devices. We expect that a detailed understanding of the kinetics of assembly and disassembly using real-time imaging coupled with simulations and experiments will go a long way towards this goal.

BIBLIOGRAPHY

1. Sigel, A.; Sigel, H.; Sigel, R. K. O., *Biomineralization: From Nature to Application*. John Wiley & Sons: 2008; p 624 s.

2. Sarikaya, M., Biomimetics: Materials fabrication through biology. *P Natl Acad Sci USA* **1999,** *96* (25), 14183-14185.

3. Baneyx, F.; Schwartz, D. T., Selection and analysis of solid-binding peptides. *Current Opinion in Biotechnology* **2007,** *18* (4), 312-317.

4. Soto-Rodriguez, J.; Hemmatian, Z.; Josberger, E. E.; Rolandi, M.; Baneyx, F., A Palladium-Binding Deltarhodopsin for Light-Activated Conversion of Protonic to Electronic Currents. *Adv Mater* **2016,** *28* (31), 6581-+.

5. Chen, A. Y.; Deng, Z. T.; Billings, A. N.; Seker, U. O. S.; Lu, M. Y.; Citorik, R. J.; Zakeri, B.; Lu, T. K., Synthesis and patterning of tunable multiscale materials with engineered cells. *Nat Mater* **2014,** *13* (5), 515-523.

6. Sano, K.; Sasaki, H.; Shiba, K., Utilization of the pleiotropy of a peptidic aptamer to fabricate heterogeneous nanodot-containing multilayer nanostructures. *J Am Chem Soc* **2006,** *128* (5), 1717-1722.

7. Zhou, W.; Schwartz, D. T.; Baneyx, F., Single-Pot Biofabrication of Zinc Sulfide Immuno-Quantum Dots. *J Am Chem Soc* **2010,** *132* (13), 4731-4738.

8. Coyle, B. L.; Rolandi, M.; Baneyx, F., Carbon-Binding Designer Proteins that Discriminate between sp(2)- and sp(3)-Hybridized Carbon Surfaces. *Langmuir* **2013,** *29* (15), 4839-4846.

9. Coyle, B. L.; Baneyx, F., A Cleavable Silica-Binding Affinity Tag for Rapid and Inexpensive Protein Purification. *Biotechnol Bioeng* **2014,** *111* (10), 2019-2026.

10. Patwardhan, S. V.; Emami, F. S.; Berry, R. J.; Jones, S. E.; Naik, R. R.; Deschaume, O.; Heinz, H.; Perry, C. C., Chemistry of Aqueous Silica Nanoparticle Surfaces and the Mechanism of Selective Peptide Adsorption. *J Am Chem Soc* **2012,** *134* (14), 6244-6256.

11. Yang, W. L.; Hellner, B.; Baneyx, F., Self-Immobilization of Car9 Fusion Proteins within High Surface Area Silica Sol-Gels and Dynamic Control of Protein Release. *Bioconjugate Chem* **2016,** *27* (10), 2450-2459.

12. Coyle, B. L.; Baneyx, F., Direct and reversible immobilization and microcontact printing of functional proteins on glass using a genetically appended silica-binding tag. *Chem Commun* **2016,** *52* (43), 7001-7004.

13. Bradley, P.; Misura, K. M. S.; Baker, D., Toward high-resolution de novo structure prediction for small proteins. *Science* **2005,** *309* (5742), 1868-1871.

14. Swift, B. J. F.; Shadish, J. A.; DeForest, C. A.; Baneyx, F., Streamlined Synthesis and Assembly of a Hybrid Sensing Architecture with Solid Binding Proteins and Click Chemistry. *J Am Chem Soc* **2017,** *139* (11), 3958-3961.

15. Hellner, B.; Lee, S. B.; Subramaniam, A.; Subramanian, V. R.; Baneyx, F., Modeling the Cooperative Adsorption of Solid-Binding Proteins on Silica: Molecular Insights from Surface Plasmon Resonance Measurements. *Langmuir* **2019,** *35* (14), 5013-5020.

16. Hench, L. L., Bioceramics - from Concept to Clinic. *J Am Ceram Soc* **1991,** *74* (7), 1487-1510.

17. Kresge, C. T.; Leonowicz, M. E.; Roth, W. J.; Vartuli, J. C.; Beck, J. S., Ordered Mesoporous Molecular-Sieves Synthesized by a Liquid-Crystal Template Mechanism. *Nature* **1992,** *359* (6397), 710-712.

18. Verwey, E. J. W.; Overbeek, J. T. G., *Theory of the stability of lyophobic colloids*. Elsevier: Amsterdam, 1948; p xi, 205 pages.

19. Israelachvili, J. N., *Intermolecular and surface forces*. 2. ed.; Academic press: London etc., 1991; p XXI, 450 p.

20. Parida, S. K.; Dash, S.; Patel, S.; Mishra, B. K., Adsorption of organic molecules on silica surface. *Adv Colloid Interfac* **2006,** *121* (1-3), 77-110.

21. Kobayashi, M.; Juillerat, F.; Galletto, P.; Bowen, P.; Borkovec, M., Aggregation and charging of colloidal silica particles: Effect of particle size. *Langmuir* **2005,** *21* (13), 5761-5769.

22. Roth, C. M.; Lenhoff, A. M., Electrostatic and Van-Der-Waals Contributions to Protein Adsorption - Comparison of Theory and Experiment. *Langmuir* **1995,** *11* (9), 3500-3509.

23. Czeslik, C.; Royer, C.; Hazlett, T.; Mantulin, W., Reorientational dynamics of enzymes adsorbed on quartz: A temperature-dependent time-resolved TIRF anisotropy study. *Biophys J* **2003,** *84* (4), 2533-2541.

24. Wahlgren, M.; Arnebrant, T.; Lundstrom, I., The Adsorption of Lysozyme to Hydrophilic Silicon-Oxide Surfaces - Comparison between Experimental-Data and Models for Adsorption-Kinetics. *J Colloid Interf Sci* **1995,** *175* (2), 506-514.

25. van der Veen, M.; Norde, W.; Stuart, M. C., Electrostatic interactions in protein adsorption probed by comparing lysozyme and succinylated lysozyme. *Colloid Surface B* **2004,** *35* (1), 33-40.

26. Wu, X. Y.; Narsimhan, G., Effect of surface concentration on secondary and tertiary conformational changes of lysozyme adsorbed on silica nanoparticles. *Bba-Proteins Proteom* **2008,** *1784* (11), 1694-1701.

27. Puddu, V.; Perry, C. C., Peptide Adsorption on Silica Nanoparticles: Evidence of Hydrophobic Interactions. *Acs Nano* **2012,** *6* (7), 6356-6363.

28. Emami, F. S.; Puddu, V.; Berry, R. J.; Varshney, V.; Patwardhan, S. V.; Perry, C. C.; Heinz, H., Force Field and a Surface Model Database for Silica to Simulate Interfacial Properties in Atomic Resolution. *Chem Mater* **2014,** *26* (8), 2647-2658.

29. Emami, F. S.; Puddu, V.; Berry, R. J.; Varshney, V.; Patwardhan, S. V.; Perry, C. C.; Heinz, H., Prediction of Specific Biomolecule Adsorption on Silica Surfaces as a Function of pH and Particle Size. *Chem Mater* **2014,** *26* (19), 5725-5734.

30. Puddu, V.; Perry, C. C., Interactions at the Silica-Peptide Interface: The Influence of Particle Size and Surface Functionality. *Langmuir* **2014,** *30* (1), 227-233.

31. Bharti, B.; Meissner, J.; Findenegg, G. H., Aggregation of Silica Nanoparticles Directed by Adsorption of Lysozyme. *Langmuir* **2011,** *27* (16), 9823-9833.

32. Wong, K.; Lixon, P.; Lafuma, F.; Lindner, P.; Charriol, O. A.; Cabane, B., Intermediate Structures in Equilibrium Flocculation. *J Colloid Interf Sci* **1992,** *153* (1), 55-72.

33. Babayan, D.; Chassenieux, C.; Lafuma, F.; Ventelon, L.; Hernandez, J., Formation of Rodlike Silica Aggregates Directed by Adsorbed Thermoresponsive Polymer Chains. *Langmuir* **2010,** *26* (4), 2279-2287.

34. Li, F.; Josephson, D. P.; Stein, A., Colloidal Assembly: The Road from Particles to Colloidal Molecules and Crystals. *Angew Chem Int Edit* **2011,** *50* (2), 360-388.

35. vanBlaaderen, A.; Ruel, R.; Wiltzius, P., Template-directed colloidal crystallization. *Nature* **1997,** *385* (6614), 321-324.

36. Ozin, G. A.; Yang, S. M., The race for the photonic chip: Colloidal crystal assembly in silicon wafers. *Adv Funct Mater* **2001,** *11* (2), 95-104.

37. Yi, G. R.; Thorsen, T.; Manoharan, V. N.; Hwang, M. J.; Jeon, S. J.; Pine, D. J.; Quake, S. R.; Yang, S. M., Generation of uniform colloidal assemblies in soft microfluidic devices. *Adv Mater* **2003,** *15* (15), 1300-+.

38. Plunkett, K. N.; Mohraz, A.; Haasch, R. T.; Lewis, J. A.; Moore, J. S., Light-regulated electrostatic interactions in colloidal suspensions. *J Am Chem Soc* **2005,** *127* (42), 14574-14575.

39. Ge, J. P.; Yin, Y. D., Magnetically responsive colloidal photonic crystals. *J Mater Chem* **2008,** *18* (42), 5041-5045.

40. Hecht, F. M.; Bausch, A. R., Kinetically guided colloidal structure formation. *P Natl Acad Sci USA* **2016,** *113* (31), 8577-8582.

41. Boal, A. K.; Ilhan, F.; DeRouchey, J. E.; Thurn-Albrecht, T.; Russell, T. P.; Rotello, V. M., Self-assembly of nanoparticles into structured spherical and network aggregates. *Nature* **2000,** *404* (6779), 746-748.

42. Forster, T., *Zwischenmolekulare Energiewanderung Und Fluoreszenz. *Ann Phys-Berlin* **1948,** *2* (1-2), 55-75.

43. Wang, X.-f., *Fluorescence imaging spectroscopy and microscopy*. Wiley: New York, 1996; p XXIX, 483 Seiten.

44. Piston, D. W.; Kremers, G. J., Fluorescent protein FRET: the good, the bad and the ugly. *Trends Biochem Sci* **2007,** *32* (9), 407-414.

45. Pawley, J. B., *Handbook of biological confocal microscopy*. 3rd ed.; Springer: New York, NY, 2006; p xxviii, 985 pages.

46. Parkhurst, K. M.; Parkhurst, L. J., Kinetic-Studies by Fluorescence Resonance Energy-Transfer Employing a Double-Labeled Oligonucleotide - Hybridization to the Oligonucleotide Complement and to Single-Stranded-DNA. *Biochemistry-Us* **1995,** *34* (1), 285-292.

47. Gonzalez, J. E.; Tsien, R. Y., Voltage Sensing by Fluorescence Resonance Energy-Transfer in Single Cells. *Biophys J* **1995,** *69* (4), 1272-1280.

48. Jonsson, T.; Waldburger, C. D.; Sauer, R. T., Nonlinear free energy relationships in arc repressor unfolding imply the existence of unstable, native-like folding intermediates. *Biochemistry-Us* **1996,** *35* (15), 4795-4802.

49. Sekar, R. B.; Periasamy, A., Fluorescence resonance energy transfer (FRET) microscopy imaging of live cell protein localizations. *J Cell Biol* **2003,** *160* (5), 629-33.

50. Stryer, L., Fluorescence Energy-Transfer as a Spectroscopic Ruler. *Annu Rev Biochem* **1978,** *47*, 819-846.

51. Ma, L. L.; Yang, F.; Zheng, J., Application of fluorescence resonance energy transfer in protein studies. *J Mol Struct* **2014,** *1077*, 87-100.

52. Pollok, B. A.; Heim, R., Using GFP in FRET-based applications. *Trends Cell Biol* **1999,** *9* (2), 57-60.

53. Nagai, T.; Yamada, S.; Tominaga, T.; Ichikawa, M.; Miyawaki, A., Expanded dynamic range of fluorescent indicators for Ca2+ by circularly permuted yellow fluorescent proteins. *P Natl Acad Sci USA* **2004,** *101* (29), 10554-10559.

54. Lunz, M.; Bradley, A. L.; Gerard, V. A.; Byrne, S. J.; Gun'ko, Y. K.; Lesnyak, V.; Gaponik, N., Concentration dependence of Forster resonant energy transfer between donor and acceptor nanocrystal quantum dot layers: Effect of donor-donor interactions. *Phys Rev B* **2011,** *83* (11).

55. Hildebrandt, N.; Medintz, I.; Algar, R., A Guide to Fluorescent Protein FRET Pairs. *Sensors (Basel)* **2016**, 16(9), 1488

56. Sapsford, K. E.; Berti, L.; Medintz, I. L., Materials for Fluorescence Resonance Energy Transfer Analysis: Beyond Traditional Donor–Acceptor Combinations. *Angew. Chem. Int. Ed.* **2006**, 45, 4562 – 4588

APPENDIX A

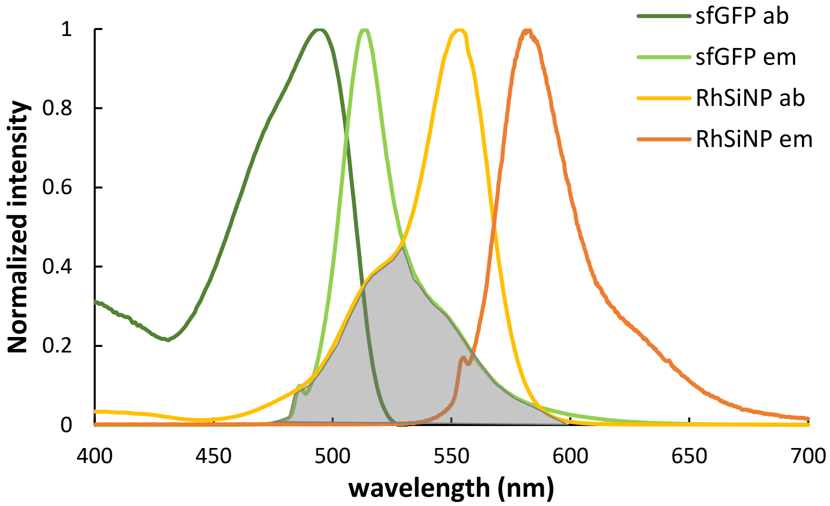

Figure A1. Normalized adsorption and emission spectra of RhSiNP and sfGFP. sfGFP had an emission peak at 512 nm when excited at 485 nm, and.RhSiNP exhibits the maximum adsorption at 553 nm. The shaded region corresponds to the overlap between the emission spectrum of sfGFP (the donor) and the absorption spectrum of RhSiNP (the acceptor).

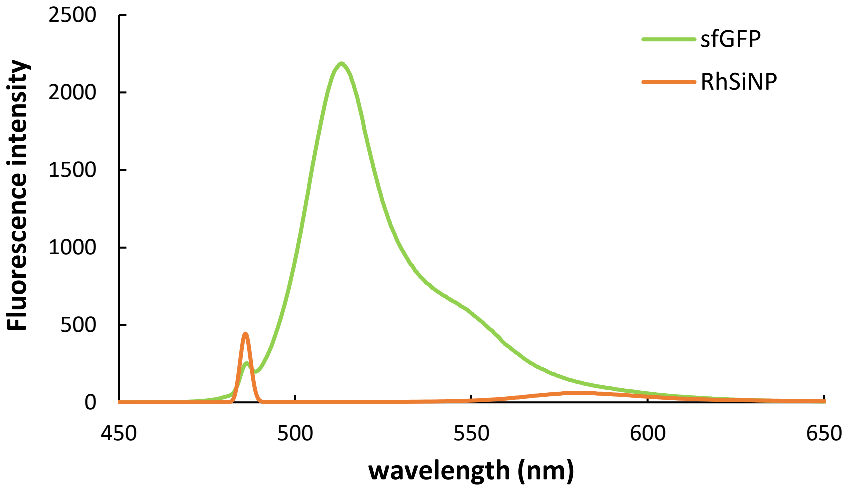

Figure A2. Emission spectra of sfGFP (5µM) and RhSiNP (1µM) upon excitation at λ_{ex}=485 nm

Table A1 Size at maximum intensity (I_{max}) and full width at half maximum intensity (FWHM) of RhSiNP (1 µM) - sfGFP::Car9-Car9 (5 µM) aggregates prepared in 20 mM Tris-HCl, pH 7.5 buffer supplemented with the indicated concentrations of NaCl.

[NaCl] (mM)	Size at I_{max} (nm)	FWHM (nm)
0	825 ± 194	500
12.5	825 ± 288	720
5	1100 ± 331	800
50	1480 ± 348	900
100	1700 ± 410	1100

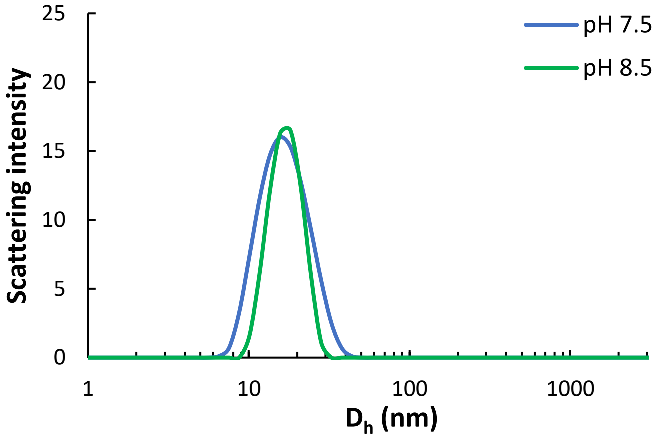

Figure A3. Size distribution of pure RhSiNP in 20 mM Tris-HCl at pH 7.5 and 8.5. Measured hydrodynamic diameters are 15 ± 7 at pH 7.5 and 18 ± 5 at pH 8.5.

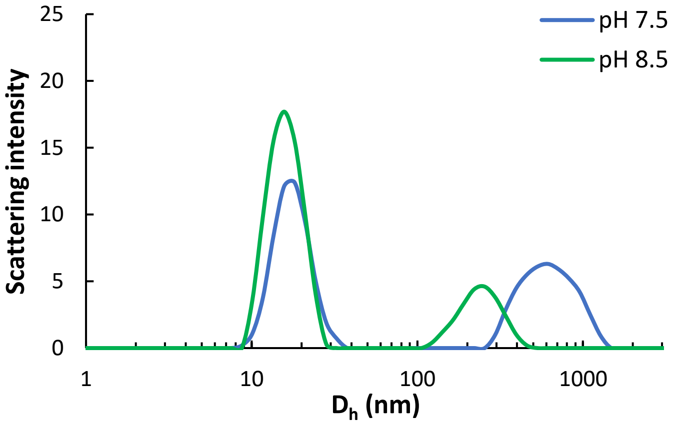

Figure A4. Size distribution of pure RhSiNP in 20 mM Tris-HCl supplemented with 100mM NaCl at pH 7.5 and 8.5